Analysis of the TOF Resolution: a "Tomography" study of the Time of Flight Detector of the ALICE Experiment at the LHC

Supervisor: **Presented by:**

Prof.ssa Silvia ARCELLI   **Nicola RUBINI**

Co-Supervisor:

Dott. Roberto PREGHENELLA

Academic Year 2016/2017

À Christine

"There are ten types of people in the world, those who understand binary code and those who don't"

Unknown

Acknowledgements

Vorrei ringraziare tutti coloro che mi hanno supportato e sopportato in questi anni, lungo il mio percorso accademico e di vita.

Per prima cosa non posso che ringraziare di cuore il mio relatore Silvia Arcelli che si è dimostrata sempre disponibile e mi ha seguito in questo lavoro con attenzione e dedizione e il mio co-relatore Roberto Preghenella che ha sempre condiviso con me il suo ufficio e la sua esperienza. Entrambi si sono prodigati per farmi sentire a mio agio e parte del gruppo, lavorare con loro è stata un'esperienza ricca ed entusiasmante.

Voglio ringraziare la mia famiglia, mio fratello Mattia, mio padre Mirko e mio nonno Franco, per aver creduto in me ed avermi permesso di essere qui oggi. Ringrazio anche tutti i miei zii e i miei cugini, che sono stati sempre una piacevole compagnia e un supporto nei momenti più duri.

Voglio ringraziare la mia compagna di vita Lisa, che ho conosciuto un settembre di tre anni fa e che mi ha accompagnato amorevolmente in questo cammino, senza mai lasciarmi. La ringrazio per tutto quello che ha fatto per me, e per tutto quello che mi dà ogni giorno.

Voglio ringraziare le mie amiche Costanza e Miriam, compagne di mille caffé, risate e qualche pianto, senza le quali non avrei resistito alla noia dello studio e alla solitudine delle sale studio. Vi ringrazio per essermi sempre vicino e aiutarmi nel momento del bisogno.

University of Bologna

Abstract

School of Science
Department of Physics and Astronomy

Bachelor's Degree

Analysis of the TOF Resolution: a "Tomography" study of the Time of Flight Detector of the ALICE Experiment at the LHC

by Nicola RUBINI

Questa tesi presenta uno studio dettagliato della risoluzione del rilevatore a tempo di volo TOF dell'esperimento ALICE, utilizzando dati di collisioni Pb-Pb del RUN 2 dell'acceleratore LHC del CERN.

È stata effettuata un'analisi dei profili della risoluzione temporale lungo i principali assi di simmetria del rivelatore (l'asse del fascio e quelli che definiscono il piano trasverso), così da evidenziare discontinuità date dalla struttura del rivelatore.

Le strutture osservate corrispondono in larga parte a effetti previsti. Le dipendenze previste sono quelle date dalla presenza di materiale, modulate dalla distanza media di traccia, che sono state confermate da una correlazione statisticamente significativa con la risoluzione. Sono anche state osservate alcune strutture impreviste, probabilmente derivanti da malfunzionamenti nell'operatività e nell'elettronica del rivelatore, che saranno oggetto di studi futuri.

Contents

Introduction

The aim of this Thesis is to study in details the timing performance of the ALICE Time-of-Flight detector, with particular emphasis on the search of systematic regularities related to experimental conditions. Given the modular structure of the TOF system and of the structures that support it, the research first focused on the symmetries of the detector. The device is in fact designed to have identical performance along super modules and among the pads at the same distance from the collision vertex. Those are the two cylindrical variables Z and Φ.

From this perspective some flaws have been found and many hypothesis about their causes were made. The aim was to confidently tell which best explained those effects. In further investigation it was found that some other variables affected the accuracy of our measurement. These premises point to a full explanation of the resolution in terms of a function of the variables supposedly affecting our measures. Attempts were made to this goal.

The importance of having a potential map for the accuracy of our detector is the ability to select the most accurate hits and to eventually emphasise their importance over less precise hits. The advantage of having an a-priori map is then to give a correct resolution to the channel. This could optimise the data taken and make the most out of previous data. Moreover there is the possibility to find systematic biases in the detector and to understand which parts of the detector work properly and which need to be reviewed.

Those factors are helpful to the ALICE experiment which works with a high average of hits per event in heavy-ion collisions and needs to properly identify as many particles as possibile. Having a theoretical error on a hit even help us extend the limits of the momentum range in which the TOF is sufficiently efficient and precise to identify a particle, as we will see later on in this work.

Chapter 1

Fundamental physics at the ALICE experiment

1.1 The Standard Model

The Standard Model (SM) is one of the most successful achievements in the theoretical understanding of subnuclear particle Physics. It describes the fundamental interactions between the elementary particles that make up the world we live in, as depicted in Figure 1.1. The Theory describes the mechanisms of the Strong, Electromagnetic and Weak interactions together with the Quarks and Leptons through the Quantum Field Theory (QFT) formalism. This description enables to picture all interactions and particles in a similar fashion, as quanta of a field, based on the concept of the classical Electromagnetic Field. This common description was achieved on the path to a grand unification theory, which we are currently seeking, a theory which should be able to describe in terms of the same essential form, in this case a field, all natural phenomena.

Recent achievements have brought us closer to that goal, in fact we already managed to unify Electromagnetic and Weak interactions in an Electroweak interaction. Nevertheless we still are missing a Field description for the Gravitation, and that is perhaps the most significant absence in the SM, together with a lack of understanding for dark matter and dark energy.

The SM introduces a binary division for the elementary constituents, based on their spin value; a half integer spin value means we are dealing with a Fermion, an integer spin value means we are dealing with a Boson. This difference is very important as it can affect the macroscopical behaviour of a system, and consists in a symmetry condition for the wave function; the wave function must be skew-symmetric when exchanging a particle for Fermions and symmetric for Bosons. These relations are formalised in the Spin-Statistic Theorem [1]

The working principle of the Theory is the charge. As we mentioned, the QFT was born on the classical idea of field and so is the concept of charge. From the XIXth century an electric charge was thought to be in those materials which interacted with electrostatic or magnetic fields, we now generalise the idea of a charge to give a particle an internal parameter to describe its possibility to interact with any fundamental force; that is the birth of the Weak charge and Strong charge. The interesting part of such a description in the case of Weak and Strong interaction is that if we can describe their force carriers in terms of a particle, they can, and will have, a non zero charge. This opens to interactions between carriers, as exemplified by gluon balls.

Other quite amazing features of the SM are the Higgs mechanism, proved in 2012 [2] and the Virtual particles. Even though it is not defined as a fundamental interaction, but rather the mean by which the particles acquire their masses, the Higgs
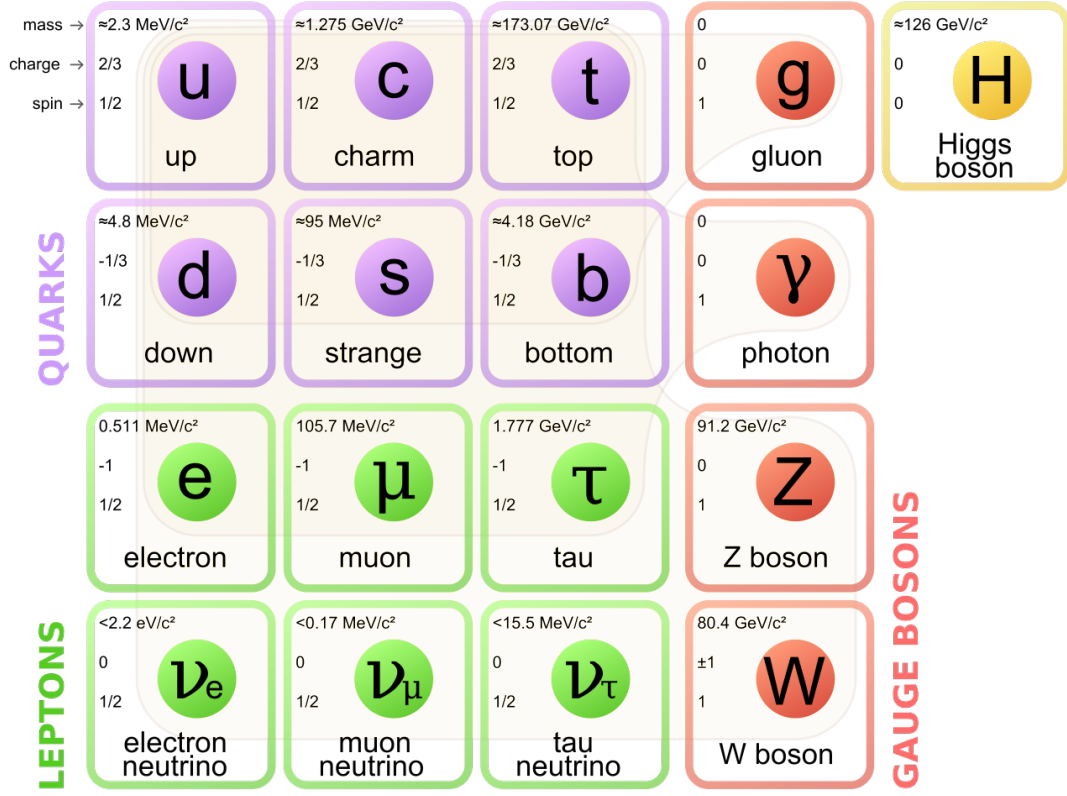
FIGURE 1.1: Particles included in the Standard Model

boson is furthermore implicated in shrinking the Weak interaction distance of effectiveness. The virtual Particles are particles with a limited life spawn according to the uncertainty principle that are exchanged in interaction processes.

1.2 The Quantum ChromoDynamics

The QCD is the part of the SM which describes the dynamics of the Strong interaction. As a QFT it makes use of *gluons*, the strong carriers, as well as virtual particles. The peculiarities of the Strong force are a unique strength and the phenomena of *confinement* and *asymptotic freedom*. It is useful to highlight that the *strength* of an interaction is beyond its naïf meaning, it in fact is an expression of the frequency of the particles exchanges, based on an intrinsic stochastic nature.

The QCD is a non Abelian Gauge Theory based on the color group $SU(3)_c$, that is an intrinsic degree of freedom of color charge, this implies a local invariance for the non commutative group transformation. This degree was introduced in the Quark Model to achieve a fully skew-symmetric wave function accordingly to the Pauli principle.

The interaction magnitude is defined by a coupling constant. To give us a scale of comparison we can evaluate the strong constant with respect to the electromagnetic one by looking at decays for certain particles.

$$\alpha_{em} = \frac{e^2}{4\pi\varepsilon_0\hbar c} \approx \frac{1}{137} \qquad \frac{\alpha_s}{\alpha_{em}} \approx 100 \qquad (1.1)$$

We eventually find that the Coupling constant is, in fact, variable and depends on the energy scale one works with and the transferred momentum, as seen in Figure 1.2. Given the probability of a process is proportional to α_s^2 we can see how it being
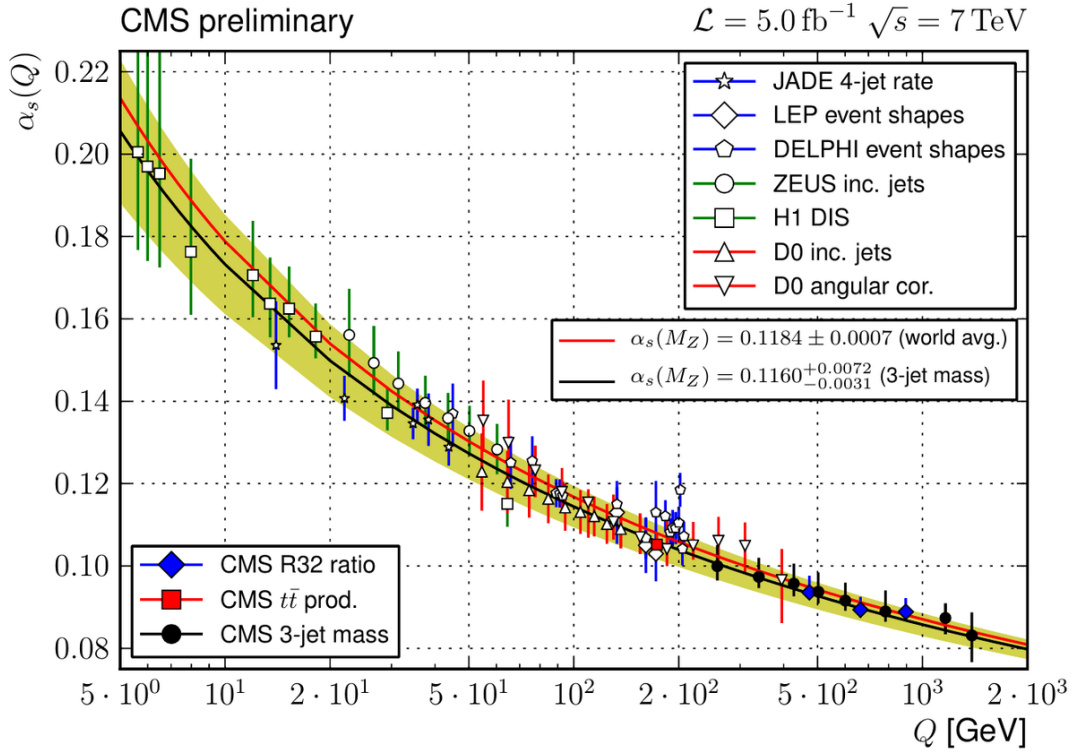

FIGURE 1.2: The α_s value with respect to exchanged momentum

nearly 1 prevents us from a perturbative approach, as we are able to do with QED, with quite astonishing results. We can evaluate the coupling parameters by studying a free particle in vacuum. We now make use of the virtual particles introduced earlier, that can produce coupled Fermions that will eventually annihilate within their time spawn. Those will affect the real charge of the particle at test and computing the screening effect will help us understand what the real charge is and how the coupling works. As we stated earlier the QED produces significant results in explaining the coupling decay over distance we observe, but the QCD works quite differently.

Let's get back to the *confinement* and *asymptotic freedom*. Those features of the Strong force are a consequence of how the virtual particles are generated in the vacuum. In fact there are couples of Fermions as in QED but, as we have seen earlier on, gluons can actually interact with each other. So self-interacting carriers come in play, inverting the screening effect of coupled Fermions, producing an anti-screening that invert the coupling strength. That is, nearby quarks feel quasi-free whilst far quarks feel a strong attraction to each other, those are the phenomena we mentioned before. The result is that in the hadron core quarks are free particles in an infinite potential box, they are strongly confined; this is the reason why we never witnessed a free quark. We nevertheless can use high energy probes to get a high transferred momentum and, according to Figure 1.2 and Eq. 1.3, reduce the coupling constant, making a perturbative approach available.

$$\lim_{q^2 \to \infty} \alpha_s(q^2) = 0 \qquad (1.2)$$

1.2.1   pQCD and Lattice QCD

We have seen so far the difficulties in calculating an exact solution for the QCD problems, mainly due to the high value of α_s. Nevertheless there are two types of approximation we can use to find some interesting results. First there is the Perturbative QCD (pQCD), which builds up an approximation to the desired degree of precision by considering more and more Feynman diagrams. This method is valid for $\alpha_s << 1$ and needs to be carefully handled, as often the integrals diverge and needs to be cut off with additional terms in a *renormalisation* and the coupling constants and fields needs to be redefined for the scale energy in use. The renormalisation group equation is

$$\frac{\partial g}{\partial \ln(\mu)} = \beta(g) \tag{1.3}$$

where $\beta(g)$ is a function describing the dependence of the constant g, where $\alpha_s = \frac{g^2}{4\pi}$, to the energy scale μ.

The interesting part of the *β function* is its sign, which tells us whether our coupling constant will rise or decrease when energy variation occurs. For the QED, the function is positive and the coupling rises with the energy scale, whilst the QCD β *function* is negative and the coupling decreases for a rise in energy scale, accordingly to the phenomena we mentioned earlier.[3][4]

At the first order we can compute an approximation for high energy ranges

$$\frac{1}{\alpha_s(q^2)} = \beta_0 \ln\left(\frac{q^2}{\Lambda_{QCD}^2}\right) \tag{1.4}$$

where q^2 in the transferred momentum, β_0 is a positive factor and Λ is a scale parameter which is ≈ 300 MeV[5] We can see here the asymptotic freedom for $q^2 \to \infty$. The second method is the Lattice QCD and it is used to compute approximate results for $q^2 \to 0$, in the low energies ranges. To evaluate the integrals at hand without divergence we can discretize the continuous field in a lattice of pace a and dimension L. After calculating the integrals on the lattice we return to the continuum field by evaluating the expressions we found for a $\to 0$ and L $\to \infty$.

1.2.2   Phase transition in QCD: The Quark-Gluon Plasma

The phase transition in QCD can be seen in Figure 1.3, in fact when the Temperature and distance, i.e. barionic density, exceed critical values the coupling constant can no longer keep the confinement and a transition to a free state occurs: the QGP forms. The transition is closely related to the flavours and masses of the quarks at hand, as the process itself is closely related to the chiral symmetry.

We can now search the critical Temperature at which the transition starts, to do so we will examine the critical temperature for relativistic pions, as those are the lightest hadrons. We will use the statistical thermodynamics principles to study our state of free quarks.

Grand Canonical Ensemble   We will make use of the Grand Canonical ensemble, as it represents an open set of particles that can exchange matter and heat with its surroundings. We start by recalling the fundamental relation

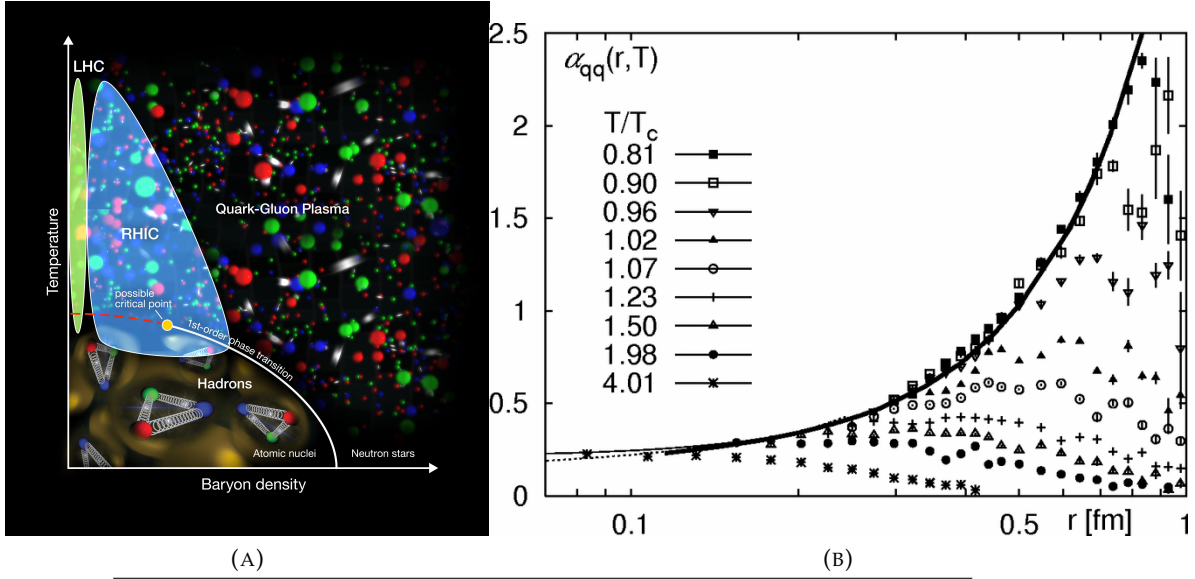$$dE = TdS - pdV + \sum_{i=1}^{n} \mu_i dN_i \tag{1.5}$$

FIGURE 1.3: (A) The Phase transition chart for QGP (B) The α_s against distance at different temperatures from Lattice QCD technique

Where we can find all the classical thermodynamic variables and μ_i, which is the energy the system takes or ceases when adding or excluding a particle of the i-th specie and is called the chemical potential.

$$\mu_i = \frac{\partial E}{\partial N_i} \qquad (1.6)$$

This potential grants the mean conservation, over major volumes or the whole system, of the i-th specie. We will focus for now on the *barionic potential*, that is the chemical potential for particles holding a barionic charge, because the barionic number $B = (n_q - n_{\bar{q}})/3$ is conserved in all SM process. The barionic potential evaluates the balance between matter and anti-matter, that is $\mu_b = 0$ calls for a perfect equality [6] for the number of particles and anti-particles.

In the case of the QGP, the high energy collisions give the particles the energy necessary to create and annihilate matter and anti-matter in such fashion that their products outnumber the initial matter, moving toward a perfect balance. Of course this is the matemathical equivalent of imposing the condition $\mu_b \to 0$[7] We now deal with two types of free particle, quarks as fermions and gluons as bosons, upon considering the appropriate statistic for each type, integrating over the whole energy spectrum we can find

$$N = g_{int} \int_0^\infty g(E) \frac{dE}{e^{\beta(E-\mu)} \pm 1} \qquad (1.7)$$

We can now consider the Semi-Classical approach, using the average over the statistical ensemble and the Uncertainty principle to get a better approximation of the reality. Moreover we suppose the energy necessary for the QGP to form is high enough to ignore the energy at rest for the relativistic particles, and get $E \approx p$. Now, from 1.7, the density for the QGP is

$$n_i = \frac{N_i}{V} = \int \frac{d^3 p_i}{2\pi} \frac{1}{e^{\beta E} \pm 1} \qquad (1.8)$$

and the energy density for the i-th particle is

$$\varepsilon_i = \frac{E_i}{V} = g_i \int \frac{d^3 p_i}{2\pi} \frac{1}{e^{\beta E_i} \pm 1} \tag{1.9}$$

Where g_i is the number of internal degrees of freedom of the particle and we have $g_b \frac{\pi^2}{30} T^4$ for fermions and $g_f \frac{7}{8} \frac{\pi^2}{30} T^4$ for bosons. The total energy density is

$$\varepsilon_{QGP} = \left(g_b + \frac{7}{8} g_f \right) \frac{\pi^2}{30} T^4 \quad \rightarrow \quad 37 \frac{\pi^2}{30} T^4 \tag{1.10}$$

The substitution was made considering that a gluon (g_b) has 16 degrees of freedom, accounting for 2 spin states and 8 color states, whilst a quark (g_f) has 12, accounting for 2 spin states, 3 colour states and 2 flavours, if we only consider *up* and *down* quarks.

If we consider a pion gas, the values for the two variables are 0 and 3, being pions scalar particles. This gives us

$$\varepsilon_\pi = \frac{\pi^2}{10} T^4 \tag{1.11}$$

Furthermore we ask to find the Pressure of the gas, that is $P = \varepsilon_\pi / 3$. At this point we need to deal with our approximations and add a term to the pressure we did not account for. That is $B \approx 0.5$ GeV/fm, we got form the Lattice QCD method. This additional term represents the confinement pressure the pions are subject to. Finally the pressure of the pion gas and QGP read as

$$P_\pi = 3 \frac{\pi^2}{90} T^4 + B \qquad P_{QGP} = 37 \frac{\pi^2}{90} T^4 + B \tag{1.12}$$

Given the transition occurs when the pressures equal each other, we can confront them and find a critical temperature at which the QGP forms

$$T_c = \left(\frac{45}{17} \frac{B}{\pi^2} \right)^{\frac{1}{4}} \approx 180 \text{MeV} \tag{1.13}$$

There are quite a few reliable phenomena which point toward the existence of the QGP, as we will see in a moment.

1.2.3 Evolution of the QGP

We can reproduce the QGP forming conditions in high-energy collisions of heavy ions. In central collisions there are many nucleons shattering one against the other in a confined space well reproducing the necessary temperature and density. The evolution of the collision goes as follow.

Hard Scattering Just a few fm/c after the collision there is the production of heavy quarks, jets and photons which in turn produce coupled leptons. As we will see later on those are the *hard probes* used to further investigate the QGP characteristic and qualities.

Fireball After a sufficient time the inelastic collisions produce a thermal equilibrium which generates a ball of free partons, a *fireball*

Freeze-out The high internal pressure call for an expansion that lowers the temperature. The quarks start to bond in hadrons at a critical temperature. Now the inelastic collisions stop and the relative abundance of the of the chemical species are fixed. The expansion continues to the point where the particles stop the elastic interactions and the strong force is not relevant to their path, they now reach the detector and the system dissolves.

1.3 Experimental data supporting the QGP hypothesis

The Experimental data supporting the QGP hypothesis are various, but are all based on secondary reconstruction of the path of the particles we detect. That is because of the short life of the QGP in the laboratory frame, as the conditions in which it can subsist long enough to be directly measured are quite hard to achieve.

1.3.1 Hard Probes

Jet Quenching A *jet* is a group of closely related particles originating from a fast parton, the Jet Quenching is a phenomenum which occurs when a *jet* is suppressed. Energetic partons are produced in hard-scatterings promptly after the nuclei collide. These partons experience the formation of the QGP and are subject to Brehmsstrahlung[1] and other energy-loss effects in the dense medium and have consequently an energy loss which can be found to be proportional to the square of the path inside the mean, a piece of information that can result in a useful way to study the QGP. As a matter of fact one can study non-interacting photons with respect to the jets to find the energy loss and consequently the suppression factor of the jet, as shown in Figure 1.4. This was first found at the RHIC, where they held central collisions Au-Au confronting them with p-p collsions correlating the suppression of π^0 and η particles. The suppression factor is represented by the fraction
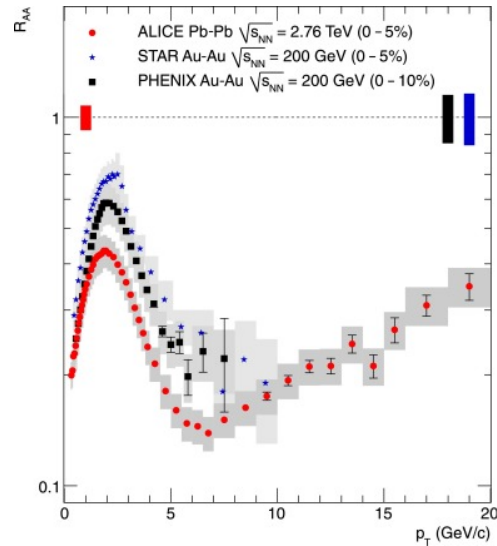

FIGURE 1.4: Comparison of RAARAA in central Pb-Pb collisions at LHC to measurements at View the MathML source $\sqrt{s_{NN}} = 200$ GeV by the PHENIX and STAR experiments at RHIC. The statistical and systematic errors of the ALICE and PHENIX data are shown as error bars and boxes, respectively. The statistical and systematic errors of the STAR data are combined and shown as boxes. The vertical bars around RAA=1RAA=1 indicate the pTpT independent scaling errors on RAARAA.[12]

$$R_{AA} = \frac{\left(\frac{d^3N}{dp^3}\right)_{AA}}{N_{collisions}\left(\frac{d^3N}{dp^3}\right)_{pp}} \qquad (1.14)$$

Quarkonia *Quarkonia* are the bound states of heavy quarks, that is particles which require a high energy to be produced, and are therefore produced a few moments in

---

[1]The radiation a charged particle emits when traveling in a mean

the collision. Later on the energy dissipates and their relative concentration remains unaltered throughout the plasma evolution. However, as a result of the shielding of the strong interaction, if the quarkonium dimensions are too little, they dissolute. Their dissolution is then a QGP proof.

Photons and Leptons   Direct photons and Leptons are essential for a good analysis of the QGP. They are emitted as the Plasma generates but do not interact with it, as we have seen earlier. This gives us a way, by analysing their spectrum, to determine the temperature of the Plasma. Together with the invariant mass of the leptons which gives us precious information about the dynamics of the matter in exam, we can have information on a wide range of variables.

1.3.2   Soft Probes

Strangeness enhancement   This was the first proof of the existence of the QGP, and was first proposed by J. Rafelski and R. Hagedorn in 1981. It is a phneomena peculiar to ion collisions, which wasn't observed in proton collisions, that can hardly be caused by an hadronic phase basis. The ions when colliding do not have any *strange* quark, so they have to be a collision by-product that in an hadronic model for production require an energy level of at least 700MeV. This is hardly in accordance to an unusual abundance of them in the ion collisions. The processes responsible for the production $s\bar{s}$ are dominated by gluon based interactions, that are abundant in the QGP. This type of production is often referred to as a *Thermal Production* to distinguish it form the Kinetic production in collisions.

Hadronic resonances   Hadronic resonances are excited states of particles, having identical quark composition but higher energy with respect to the ground state particle.Each ground state hadron may have several excited states; several hundreds of resonances have been observed in experiments. They have an extremely short life, about $1\,\mathrm{ys}$, so they need to be studied through their decay via Strong interaction. In heavy ion collisions they generate in the Fireball expansion, and decay before getting through. This means that the decay products have to interact with the QGP and it is impossible to use their invariant mass to identify the particle that produced them. Nevertheless they can regenerate in the freeze-out phase with secondary collisions and studying this process in contrast to re-scattering gives us information on their cross-section. The study of resonances and their mean life can give us some insight on the phases the QGP goes through.

Light nuclei production   In the collision there is a small production of light nuclei and anti-nuclei in the transversal direction of the beam, that cannot be coming from the scattering. We think they might come from in the *Kinematic Freeze-out*, as earlier stages could not produce low energy systems. Their analysis is then a useful probe in understanding temperature, barionic denisty, and spatial extention of the hadronic system.

Chapter 2

A Large Ion Collider Experiment

A Large Ion Collider Experiment (ALICE) is one of the main experiments at CERN, and it is one of the main four located on the Large Hadron Collider (LHC) ring (Figure 2.1) together with CMS, ATLAS and LHCb.

The LHC was first ran in 2008 and was born on the ashes of the previous accelerator, the Large Electron-Positron (LEP) collider, dismantled in 2001. The main new feature of LHC is its power of acceleration: it can make particles reach velocities almost the speed of light. This is achieved by connecting the previous accelerators to sum their impact on the particles step by step, before entering LHC where they will be brought to the collision energy. It is worth noting that the beams are focused, kept at a quasi-perfect vacuum, at temperature on the premises of the absolute zero and have a good luminosity to maximise their efficiency in collisions. Moreover the ALICE detectors are optimised for heavy ion collisions, typically Pb-Pb, where the number of particles created in each collision is significantly higher than those in p-p collisions, which are studied in the other experiments, with a design center of mass energy per nucleon pair of $\sqrt{s_{NN}} = 5.5$TeV. Up to now, the energies reached were 2.76 TeV and 5.02 TeV.

The purposes of the four experiments vary, from CMS and ATLAS looking to expand our knowledge and understanding of the SM and go beyond it, the LHCb examining the flavours of particles through decay channels and ALICE seeking proofs and features of the QGP.

2.1   ALICE Detectors

The ALICE collaboration goal is to study the QGP as a new state of matter, but to accomplish that one must overcome several technical difficulties; the high temperatures do not allow detectors in proximity of the collision vertex for example. To solve those issues and make the most of the information gathered in the collisions it is vital to properly identify each and every particle exiting the QGP as it cools down and re-establish the strong confinement.

To do so, ALICE set up a special set of detectors in addition to the ones used in other LHC experiments. In fact those identify particles by the characteristic signature they leave in the detectors, layered pointing outward the collision vertex, in a cylindrical symmetry. First a tracking system, then an electromagnetic and finally a muon system. The whole apparatus is embedded in a magnetic field ($\sim 0.5\,\mathrm{T}$) that bends the particles trajectories, depending on their momentum and charge. A crucial role in the context of particle identification in ALICE is covered by the Time of Flight Detector which provides us with the particles speed, which can be combined with the momentum we measured in a previous step to determine the mass of the particle.
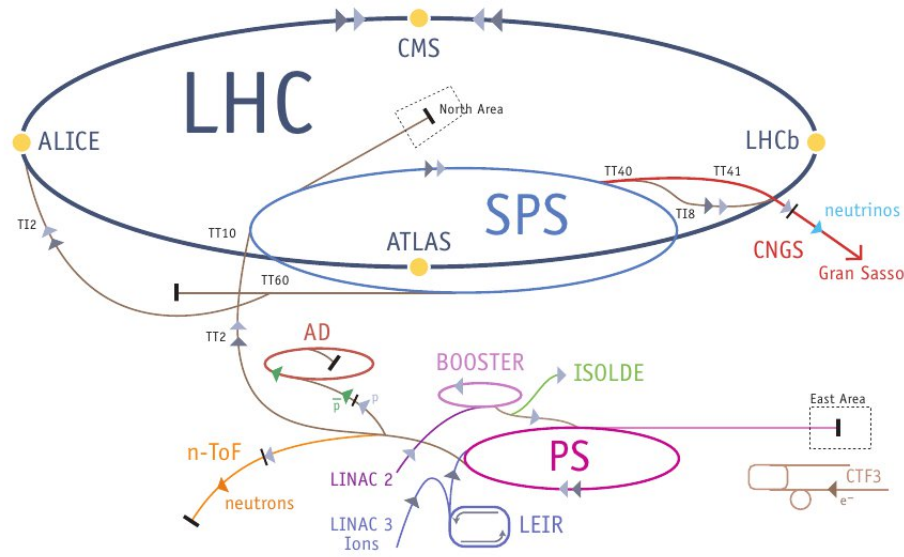
FIGURE 2.1: A schematic representation of the CERN accelerators

The main problem with the ALICE experiment is the high production of particles, over a hundred times more the ones in other LHC experiments, and it is very important for this experiment to track the most particles. That is why the whole set up is optimised to have the maximum acceptance and detection efficiency. To this purpose ALICE is designed to sustain a multiplicity density of 8000 per rapidity unit, covering two rapidity units. The maximum observed in Pb-Pb collisions so far is more than 2000 per rapidity unit.

It is designed to sustain a multiplicity of 4000 charged particles, and has been tested for twice this number. The detector is cylindrical around the vacuum tube the beam travels in, covering a polar angle of $\pm\frac{\pi}{4}$ and we can get an idea of the structure in Figure 2.2.

2.1.1   The ALICE Structure

The ALICE Structure follows a cylindrical symmetry as seen in Figure 2.2. It builds up in consecutive layers each devoted to a particular measurement, to keep track of the particle path in the detector and to account for all the energy loss of non-reconstructed vertices.

The Inner Tracking System (ITS)   The ITS is the first detector from the collision vertex and it is made from six concentric cylindrical detectors. The layers are coupled in two Silicon Pixel Detector, two Silicon Drift Detectors (SDD) and two Silicon Strip Detector (SSD), going outward. Its main purpose is to help the TPC tracking the primary and secondary vertices of the collisions, improve the TPC momentum resolution for p_T higher than 100MeV and measures the momentum of low energy particles from their energy loss. Its resolution is as high as 100 μm**[8]**

The Time Projection Chamber (TPC)   The TPC is the real tracking system in ALICE, and works similarly to the ITS. In fact it measures the specific energy loss of the particles to identify them, having a high resolution on high momentum charged
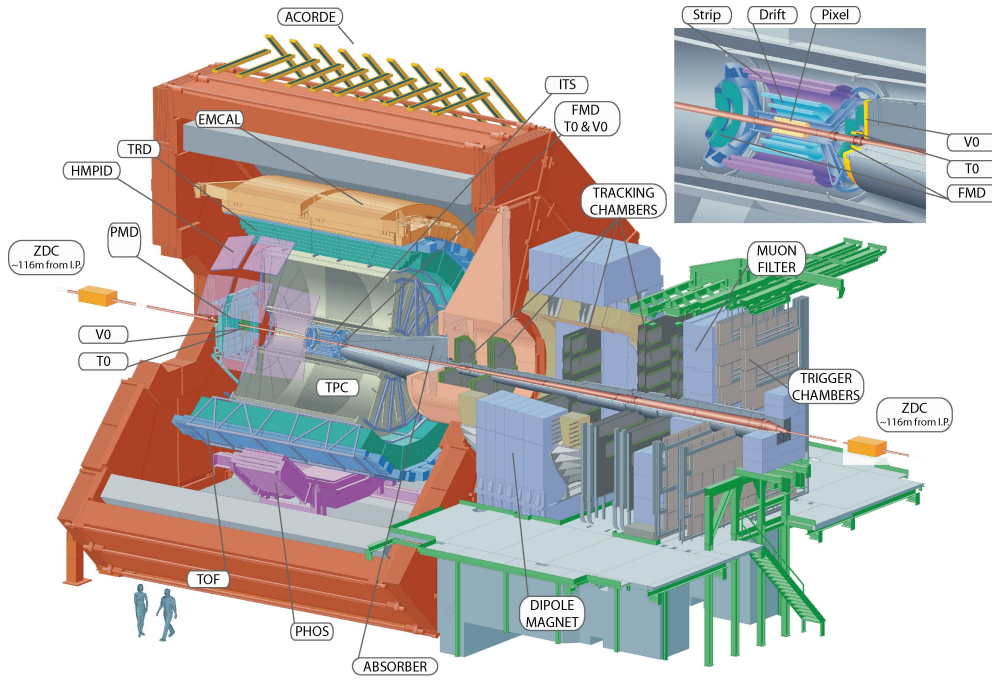
FIGURE 2.2: The ALICE detectors layered structure

particles tracking. It is a cylindrical system ranging from 0.85m to 2.50m from the beam pipe which grants an adequate track length for the measurements. This results in a good resolution for the energy loss, that is less than 10%, which in turn gives an efficient identification of particles having $p_T \leq 1$GeV, that is at least a 3σ separation.

As we mentioned before the ITS is used as a compensation for TPC dead zones, and in fact the TPC misses 10% ca. of the tracks that are instead traced in the ITS.[9]

The T0 Detector The detector is composed of two arrays of Cherenkov counters, T0C and T0A, along the Interaction Point axis, one opposed to the other. Each array has 12 cylindrical counters equipped with a quartz radiator and a photomultiplier tube. The T0 detector was the first ALICE detector to be turned on and during Run 1 it provided trigger signals 625ns after the collision time.
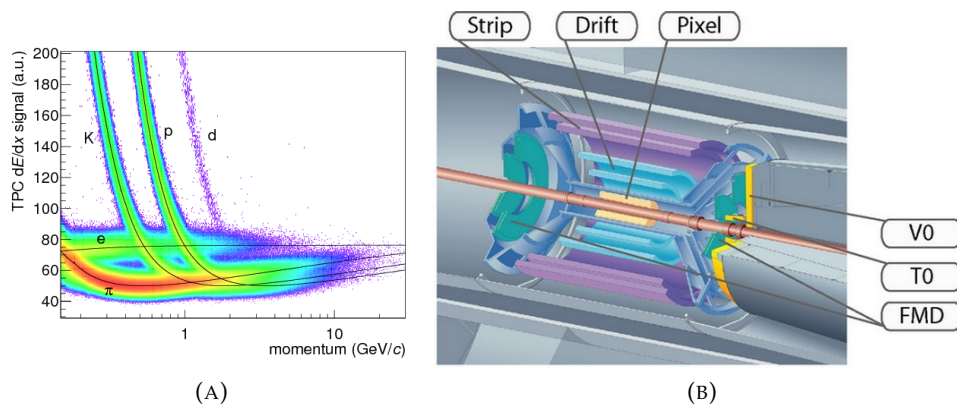

FIGURE 2.3: (A) The TPC results on particles energy loss. (B) The ITS inner structure.

The Transition Radiation Detector (TRD)   The TRD improves the momentum resolution and has an excellent capability for electron identification: it in fact tracks and identifies electrons for momenta higher than 1GeV. The detector surrounds the ITS and TPC cylindrically from 2.9m to 3.7m and extends to 7m along the beam axis. It is divided in six layers which arrange 522 chambers that include a radiator, front-end electronics and cooling systems, having an average size of 135cm x 103cm x 12cm.

The system used is quite simple, it uses the fact that a charge particle going through a separation surface between two materials having different dielectric constants emits a characteristic radiation.

The Photons Spectrometer (PHOS)   The Spectrometer is specialised in distinguishing the photons coming directly from the QGP from the background generated by the EM decays. It has 17000 pads and uses a scintillator crystal of $PbWO_2$ cooled at $-25\,°C$.

The Forward Muon Spectrometer (FMS)   The FMS is in the forward region of the detector (2.5<η<4) and is used to detect coupled μ_+ and μ_- that are useful when computing their invariant mass, to deduce their mesonic resonances of heavy quarks.

2.1.2   Particle Identification in ALICE

As mentioned before particle identification is very important at ALICE, in fact there are two detectors completely dedicated to this purpose.

The Time of Flight (TOF)   The time of flight detector is used to measure the time of flight of charged particles with intermediate p_T, roughly 1 GeV, through a fixed path to determine their velocity. It will be deeply investigated further on.

The High Momentum Particle Identification Detector (HMPID)   The HMPID is dedicated to detecting hadrons with high p_T and is a Ring Imaging Cherenkov detector (RICH) located at 4.9m from the beam pipe. It is divide in seven modules, covering an active region of about $10m^2$. Its purpose is to extend the TOF, ITS and TPC momentum range. This detector works on the principle that particles going through at high speed cause the emission of Cherenkov photons which are detected by a photons counter.

2.2   The Time Of Flight Detector

The Time of Flight (TOF) detector will be the main focus of this theses. Its purpose is to identify charged particles like Pions, Protons and Kaons, within a momentum range from ~ 0.3 GeV to ~ 2.5 GeV. Its power of discernment for charged particles is a very suited solution to particle identification in its range of effect. That enhances our particle identification possibilities with respect to an energy loss approach and covers $\approx 97\%$ of the particle generated in our events. The other 3% is covered by a Cherenkov method, more effective in high momentum ranges.
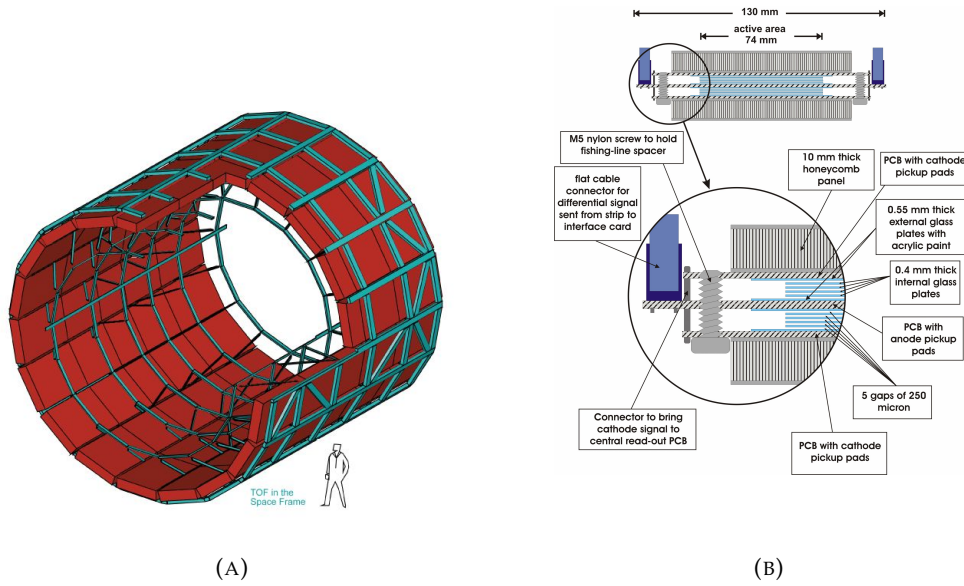
FIGURE 2.4: A schematic representation of the TOF structure and spaceframe (A) and a close up on a MRPC (B)

The Multi-Resistive Plate Chamber   The MRPC is a stack of resistive plates filled with gas between them as in Figure 2.4. They have two external cathodes and an internal anode. The functioning principle is simple: the passing particle ionise an electron and the latter is accelerated by the static electric field and now has enough energy to ionise again, and so on, in a process called the avalanche effect, the signal is then picked up by external electrodes, called *pickup pads*. Intuitively, the efficiency of the single RPC improves as the gap widens, but the resolution worsen, and viceversa when reducing the gap. The MRPC combines a width that grants a high efficiency while stacking narrow gaps that grants a very precise measure, in an escamotage that can accomplish an average intrinsic resolution measured in test beams to be better than $\sim 50\,\mathrm{ps}$.

The Detector Structure   The detector is almost cylindrical, having 18 plates, called sectors or supermodules, along the coordinate φ. The cylinder extends over $7.4\,\mathrm{m}$ along the Z axis and has a radius ranging from $3.7\,\mathrm{m}$ to $4\,\mathrm{m}$ for the inner and outer part respectively. Supermodules have five inner structures called modules, that are groups of MRPC:

- Central module is $1.14\,\mathrm{m}$ long and has 15 MRPC

- Intermediate module is $1.47\,\mathrm{m}$ long and has 19 MRPC

- External module is $1.78\,\mathrm{m}$ long and has 19 MRPC

The detecting component is the MRPC strip, which has 96 indexed pads, each measuring a time, as shown in Figure 2.4. Their disposition with respect to the cylinder axis is progressively tilted from $0°$ to $45°$ to maximise their efficiency and coverage of the particle production. Each pad has a coverage area of $3.5 \times 2.5\,\mathrm{cm}$.
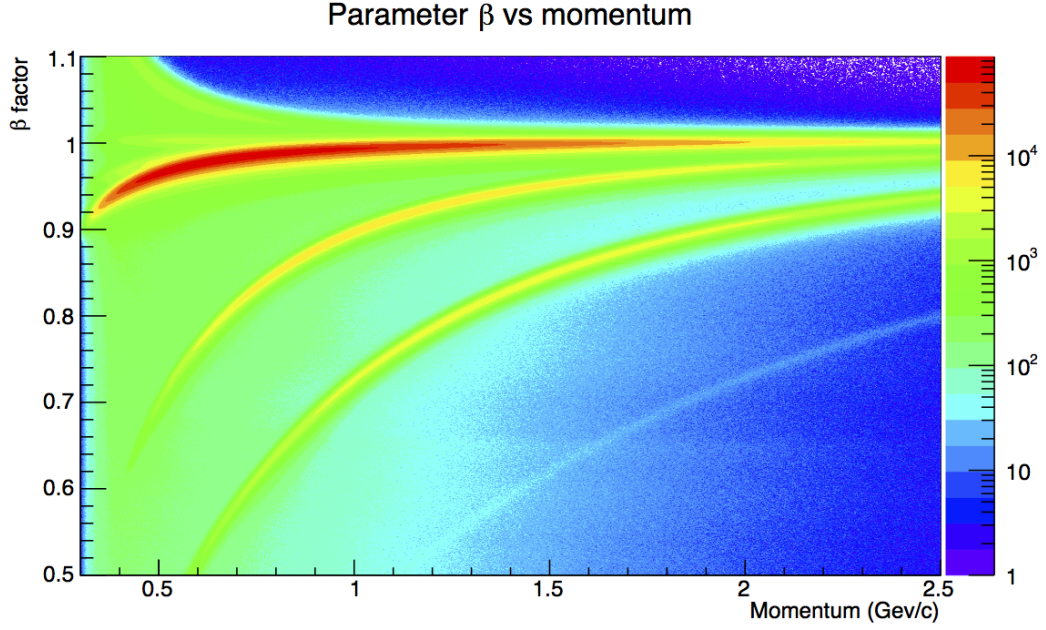
FIGURE 2.5: The β factor against the Momentum

Particle identification   Having measured the Time of Flight for the particle, knowing the track length and getting from previous detectors its momentum one can easily find out the particle mass, that is identify it. We may now wonder about the precision of the identifying problem, and to evaluate that we must overlook the process. On a preliminary note, Figure 2.5 already gives us a piece of information: our power to identify particles decrease as the momentum increase.

We will work in Natural units for simplicity, and first recall

$$v = \frac{L}{T} \quad \gamma = \frac{1}{1 - v^2} = 1 + \frac{p^2}{m^2} \quad p = mv\gamma \quad E = \gamma m \quad E^2 = m^2 + p^2 \tag{2.1}$$

which combined give us the particle mass and its error

$$m^2 = p^2 \left(\frac{t^2}{L^2} - 1 \right) \qquad \frac{\delta m}{m} = \sqrt{\left(\frac{\delta p}{p} \right)^2 + \left(\gamma^2 \frac{\delta L}{L} \right)^2 + \left(\gamma^2 \frac{\delta t}{t} \right)^2} \tag{2.2}$$

If we now focus on the time contribution to the error, we can indeed see a dependence on momentum by the means of γ. We now try to evaluate the separation of times for particles with the same momentum on a equally long path.

$$t = L\sqrt{1 + \frac{m^2}{p^2}} \quad \approx \quad L\left(1 + \frac{m^2}{2p^2} \right) \quad \rightarrow \quad \Delta t = \frac{L}{2p^2} \Delta m^2 \tag{2.3}$$

The first approximation is the Taylor expansion for $p \rightarrow \infty$, the right part of the equation is the time difference between the two particles. Those results are better shown in terms of standard deviation by the relation

$$n_\sigma = \frac{\Delta t}{\delta t} \tag{2.4}$$

that gives us a standard scale of the degree of separation we can expect from our detector. **[10]**

Chapter 3

The Time Of Flight Resolution

In this Chapter we will be analysing the performance of the TOF Detector as to determine wether there are some inefficiencies or systematic fratures in the measurement processes abducted by the detector's geometry, internal structure or electronics malfunctioning.

To do so we will introduce the expected time t_{exp} of hit for a test particle and use it to calibrate our data so as to focus on the sole resolution of the single channel. Once we have the resolution it will be possibile to see how it behaves in regards to the structure and disposition of the detector.

The data we will use in this analysis come from the LHC Run 2 for Pb-Pb collisions at $\sqrt{s_{NN}} = 5.02$ TeV. The analysed sample correspond to about 4.3 M events collected with a trigger configured to selected hadronic collisions with high efficiency. The average number of reconstructed track hits on the TOF is ≈ 225.

The Monte Carlo simulations are fully simulated events in a detailed simulation of the experimental environment, reproducing ALICE detectors emplacement and material density. They are simulated pions generated in the central region of the detector, where the primary collision vertex is located in the most accurate way possible so as to reproduce a real event. Pions are uniformly produced over the solid angle so as to cover all the central barrel detector surface, with a momentum range that covers uniformly 2.2 GeV from 0.3 GeV to 2.5 GeV. The magnetic field effect and the energy loss is also included and simulated for the particles. For the Material MC simulation the material is assigned integrating the density along the track, resulting thusly in $\mathrm{g\,cm^{-2}}$.

3.1 The TOF Calibration

The Calibration process is essential to keep an efficient Detector that is able to provide a high precision time measure. There are many time variables involved in the TOF calibration. The main issue is finding the calibration offsets on the single pad, namely the value that ensures the agreement of measured and expected time of flight, on a statistical basis. The calibration offsets are determined as the mean of the single-channel distribution

$$\Delta_{t_\pi} = t_{measured} - t_{exp\pi} - t_0 = t_{TOF} - t_{exp\pi} \tag{3.1}$$

The expected time parameter $t_{exp\pi}$ is our theoretical estimate for the time the pion hit the pad, and is crucial to determine if the detector has any offset or unusual time measurements distribution. It is built on the momentum and mass of the pion, considering step by step its trajectory from the interaction vertex to the TOF detector, taking into account the energy loss caused by the interaction with the previous

detectors. Recalling equation 2.3, the parameter is simply

$$t_{exp\pi} = \sum_k \Delta_{i;k} = \sum_k \frac{\Delta L_k}{p_k} \sqrt{p_k^2 + m_i^2}$$ (3.2)

considering the momentum unchanged along the small step.[11] An important point to stress is this new variable we introduced is specific for pions, meaning it could bias the measurements for other particles if used. As a matter of fact that is not just a possibility, as we can see in Figure 3.2 where the second and third line refer to Kaons and protons, for which our expected time shifts the Δ_{t_π} differently according to the momentum. The Figure also highlights how the higher the momentum, the smaller the differences between Pions and Kaons become. Pions are taken into consideration because they are the most prolific particles in heavy ions collisions as they represent 80% of the total generated and are the less massive, which is advantageous for a more precise reconstruction of their track, due to a minor energy loss through previous detectors and structures. Moreover, being low-mass, they reach velocity saturation ($\beta = 1$) earlier, making the momentum reconstruction resolution affect the expected time of flight in a negligible way already at relatively low momenta.

The time zero parameter t_0 is the reference for the time of flight measures, as it indicates the time of the collision. It is given by the T0 detector with a precision on ~ 25 ps. The TOF can independently determine t_0 based on a χ^2 minimisation algorithm using the measured and expected time of flights.

The TOF resolution is then, based on the above,

$$\sigma_{TOF}^2 = \sigma_{t_{exp\pi}}^2 + \sigma_{t_0}^2 + \sigma_0^2$$ (3.3)

where we introduce σ_0 as TOF intrinsic error on measures.

3.1.1 The Fit Function

The TOF resolution is to be evaluated fitting Figure 3.1 with a custom function for TOF signals that considers the presence of an exponential addition to the right part of the gaussian model. It's important to specify that we used here a cut on the Momentum of the particle examined as the momentum affects the precision of the measurement. Of course we must elaborate an expected time for a single particle, in our case pions, in order to con-

FIGURE 3.1: Deviation of Measured time from expected time at 1.5 ± 0.05 Gev

sider all variables in the Laboratory that may affect the results, that is the $t_{\exp\pi}$. As we can see in Figure 3.4 there is a disturbance in the high momentum range over $\approx$
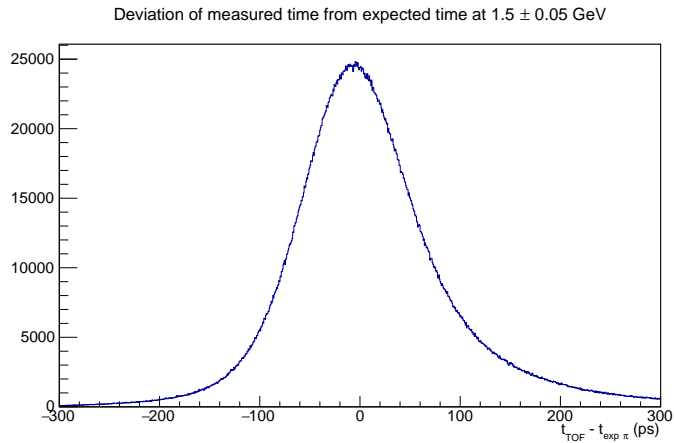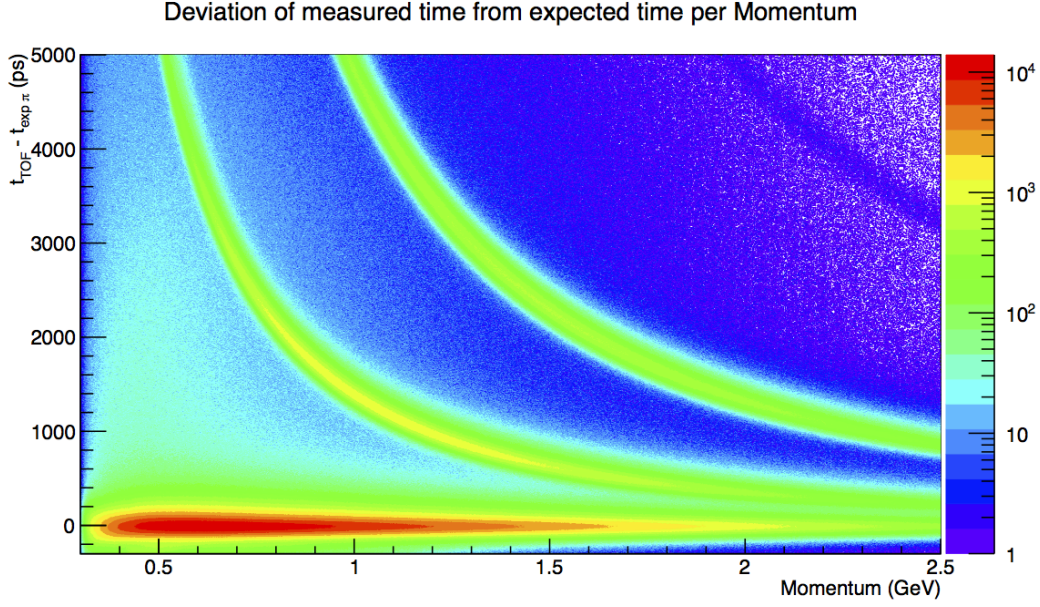
FIGURE 3.2: Characteristic time $t_{TOF} - t_{exp} - t_0$ against Momentum

1.8 GeV and one must account for the presence of a deformation of the exponential tail, brought by the proximity of the Kaon signal.

$$f_{fit}(\Delta_{t_\pi}) = \begin{cases} \Delta_{t_\pi} \leq ([3]+[1]) & [0] \times e^{-\frac{1}{2}\frac{(\Delta_{t_\pi}-[1])^2}{[2]^2}} \\ \Delta_{t_\pi} > ([3]+[1]) & ([3]+[1]) \times e^{-\frac{1}{2}\frac{(\Delta_{t_\pi}-[1])^2}{[2]^2}} \times e^{-[3]\frac{\Delta_{t_\pi}-[3]-[1]}{[2]^2}} \end{cases} \quad (3.4)$$

Over the Kaon proximity limit we introduced a gaussian fit to elude the Kaon contribution.

3.2 The Resolution Dependencies

Now that we know the processes which let us measure the Resolution of a given signal, either from a single channel or a group of channels, we can start our search for variations and investigate their causes.

First we can make some assumptions on equation 3.3. The contribution of σ_0 and σ_{t_0} may be considered as constant, while we know for certain that there is a dependence on momentum for the $\sigma_{t_{exp}}$, recalling 3.2.

$$\sigma_{t_{exp}} = \sum_k \left(\frac{\Delta L_k}{p_k} \sqrt{p_k^2 + m_i^2} \right)^2 \quad (3.5)$$

We can then see how the resolution worsen with lower momentum in Figure 3.4 and in Figure 3.3

3.2.1 Geometric Patterns

We saw earlier how the momentum affects the Resolution as a whole, without requiring to focus on any particular part of the Detector. We can now ask ourselves
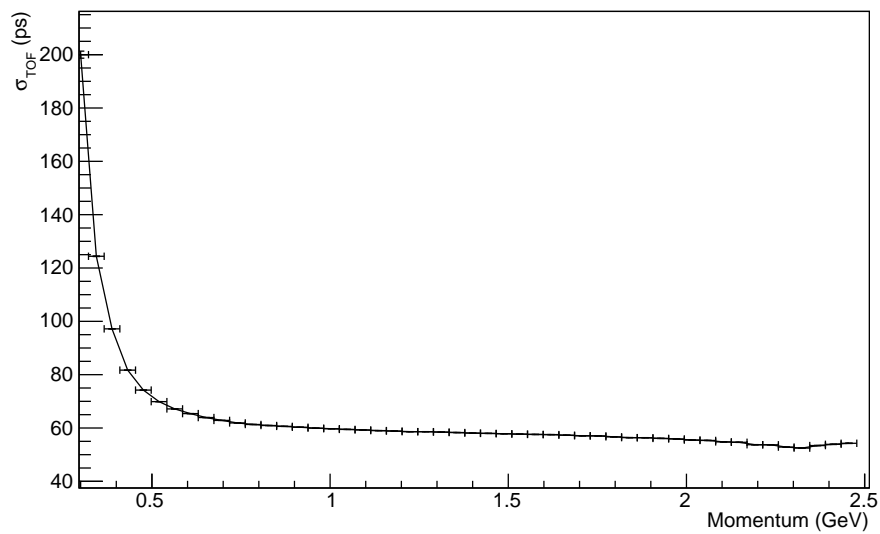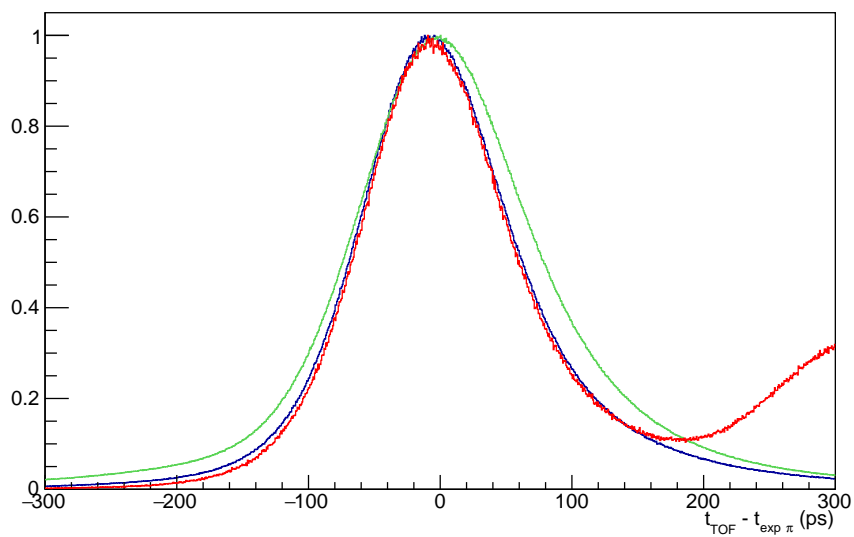
FIGURE 3.3: The resolution against the momentum

FIGURE 3.4: Comparison between the Δ_{t_π} signal at 0.5 GeV (Green),
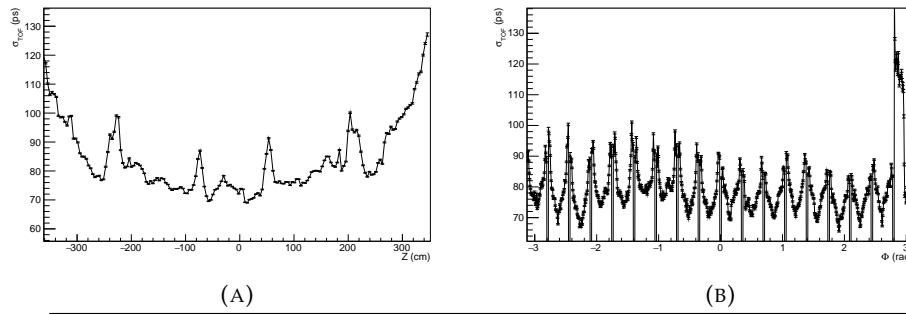1.5 GeV (Blue) and 2.5 GeV (Red)

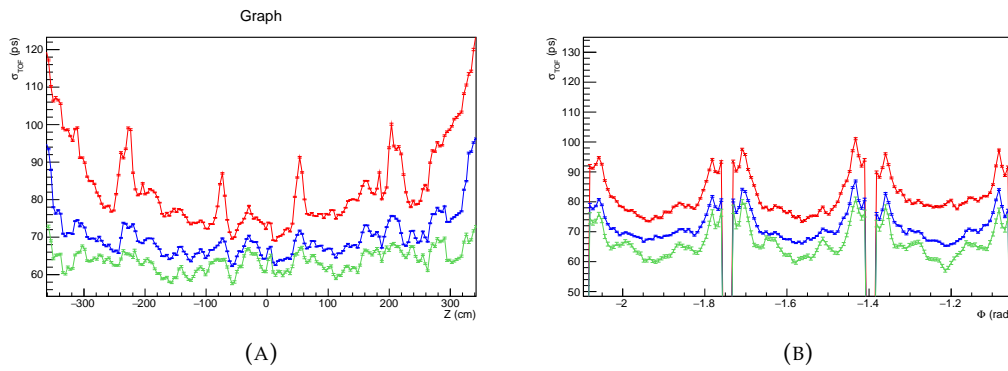FIGURE 3.5: The Resolution along Z and φ cylindrical coordinates, at 0.5 GeV

FIGURE 3.6: The Resolution along Z and φ (zoom) cylindrical coordinates, at 0.5 GeV (red), 0.8 GeV (blue) and 2.0 GeV (green)

wether there will be any fluctuations between different zones that could lead to discover new variables affecting our Resolution.

Our structure is cylindrical, so it is natural to exploit the symmetries a cylinder provides to get a first glimpse on the supposed differences we could expect. To do so, we will plot the Resolution against the Z and φ cylindrical coordinates, slicing data at 0.5 ± 0.05 GeV so as to eliminate the momentum impact.

Figure 3.5 clearly shows that along both directions there are periodic structures and local dysfunctions. Perhaps the most obvious and clear anomaly is the 8th sector, which has an offset of $\approx 30\,\mathrm{ps}$ with respect to the others. This lack of symmetry hints that this might be a first anomaly in the detector functioning, rather than a systematic dependence of the Resolution on a physical variable. As for the analysis purpose we will suppose the 8th sector, located in $2.80 \leq \varphi \leq 3.14$, as out-of-trend and it will consequently be excluded in further processing.

We can now focus on the recurrence of spikes in both profiles. There is a clear difference between the two, as the Z profile highlights a parabola on top of which the spikes are formed, while the φ profile only has recurring spikes on a flat background. Those are important remarks as they suggest the presence of a systematic dependence that is stronger along Z and weaker or absent along φ.

We shall now evaluate how the dependence is related to the momentum, as we know it affects the resolution. That is done in Figure 3.6, which hints that the variable we are looking has a momentum modulated dependence. This leads us to think of the material the particle goes through before hitting the detector as the variable at
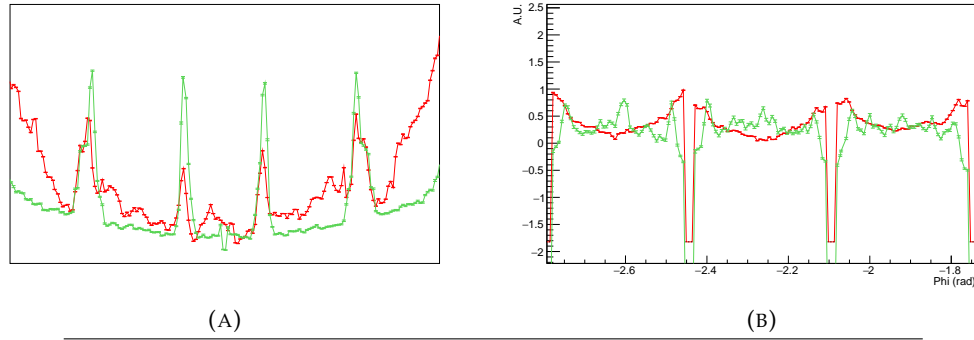
<div align="center">(A)</div>

<div align="center">(B)</div>

FIGURE 3.7: The Resolution (Red) and material density (Green) along
Z and φ (zoom) cylindrical coordinates, at 0.5 GeV

hand here. Once we suppose that the material is the variable impacting the Resolution, it is easy, confronting Figure 2.4, to see that the spikes we see in both coordinates are non other than the spaceframe's metal bars, which further convince us that the material has in fact a major impact on the Resolution.

3.2.2 The Material action

We derived from general observations that there might be a Material impact onto the resolution. We now confront the resolution to the material density along the coordinates, using a fast simulation to get a first glimpse at the problem. That is done in Figure 3.7.

The patterns in Z are similar and thus we can safely say there is some kind of correlation between the two variables, even though those in ϕ exhibit some out-of-trend behaviour. Now, to evaluate their correlation, we may simply couple the two graphs, that is connect the two graphs Y values trough their common X values. This should give a graph plotting the correlation between Material and Resolution.

This first approach was unsatisfying and gave virtually no other results as can be seen in Figure 3.8. The best result was undoubtedly given by the Z correlation, whilst the φ is again out-of-trend, which strengthen our first guess of it having intrinsic effects masking the dependence we are looking to establish. So as to refine the analysis we refined the method, applying it directly on the single channel. That is we keep record of the material a particle goes through per momentum slice per channel and plot the average material per momentum slice per each channel. Having done so, we can now associate directly a material value to the channel itself, so as to build a two-dimensional histogram of material against the characteristic variable $t - t_{exp}$, for later fitting. As a result, the correlation is much clearer and quantifiable, as we can see in Figure 3.9.

$$\sigma_{TOF} = c_{\mathsf{m},\mathsf{p}} \frac{\mathsf{m}}{\mathsf{p}} \tag{3.6}$$

where p is the Momentum and m is the material, which could be very useful to find further malfunctions in the detector or to improve its accuracy. Upon trying to Fit such a function we meet with some unsatisfying results. We now try to investigate the reasons why our model is not accurate enough to satisfyingly fit the data. To do so we once again try to get some information from a qualitative approach to the graphs. In particular, we can see how the model along Z must sharpen the background parabola to match the resolution pattern. This hints there must be another
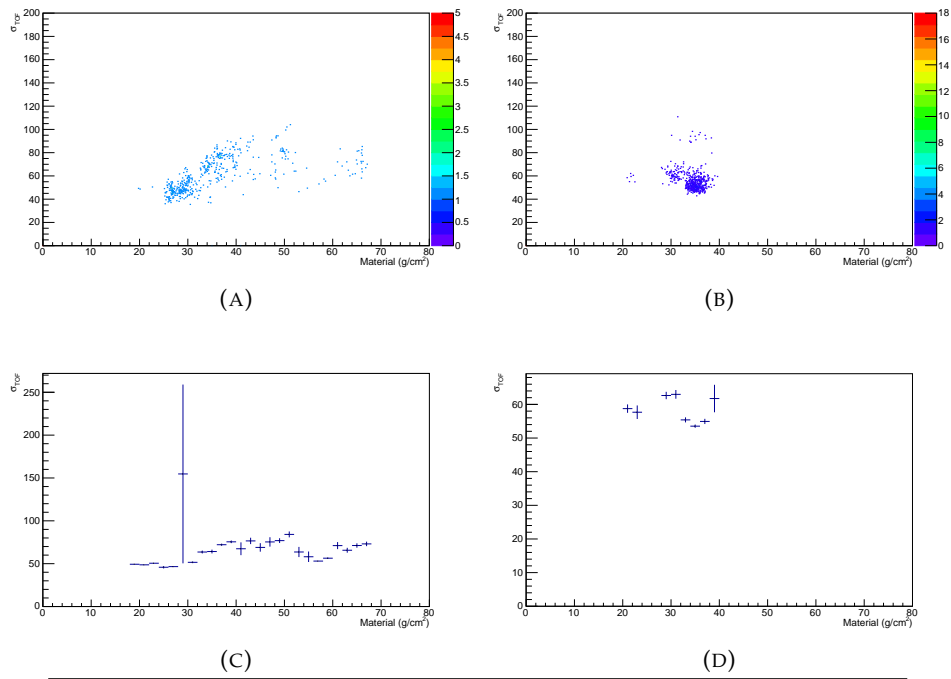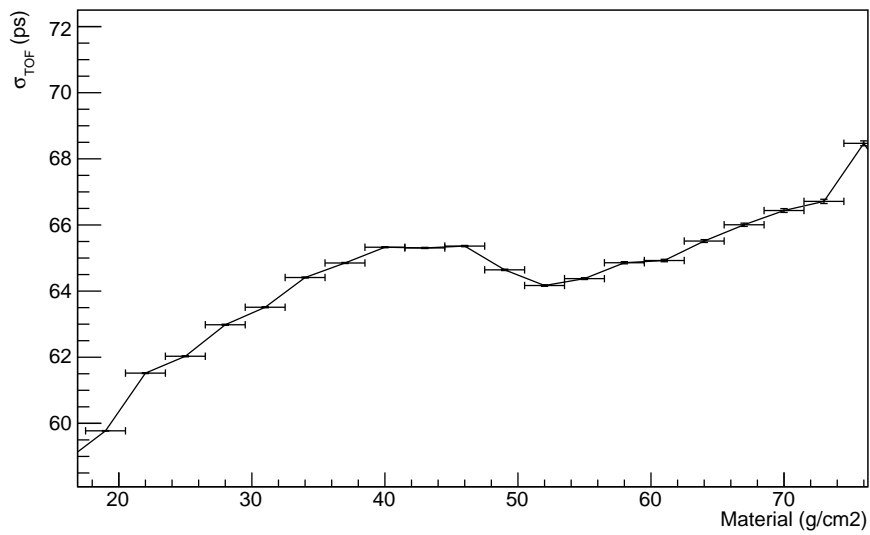
FIGURE 3.8

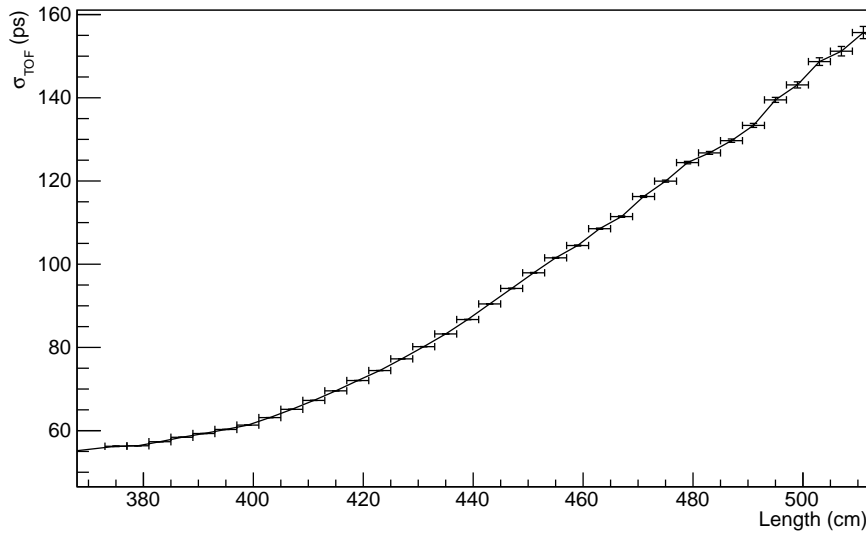FIGURE 3.9: The resolution against the material density on track

FIGURE 3.10: The resolution against the track length

variable affecting the detector's precision, in particular this variable is expected to have a trend similar to the material's, as it affects greatly Z and weakly φ. Furthermore it is of greater impact for high values of Z, so the natural variable to consider is the Track length.

Furthermore we examine the discrepancy along φ where there are cyclic spikes that do not match any variation in the material. We suppose those are another systematic error derived from other causes and focus on the central part of our pattern. On a similar note we find an unexpected bump in the central region along Z and upon taking a closer look the spikes along Z are somewhat different from those expected from the material map.

3.2.3   The Track Length action

To examine the possible dependence onto the Track Length we proceed in an analogous way, linking a mean track length to the channel and using it to plot the resolution against the track length. The results are shown in Figure 3.10.

We can now update our Formula as

$$\sigma_{TOF} = \sqrt{c_{p,l}^2 \frac{l^2}{p^4(1 + \frac{p^2}{m_\pi^2})} + c_{m,p}^2 \frac{m^2}{p^2}} \tag{3.7}$$

where l is the Track Length. This dependence is coherent with the data we plotted in Figure 3.10 and is a natural addition to the function given the results worked out in 3.5.
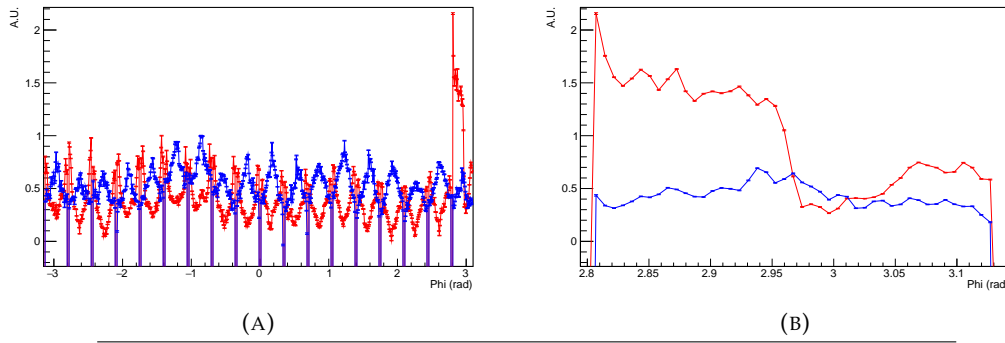
FIGURE 3.11: The Resolution (red) and Simulated Resolution (blue) along φ and a Zoom on the 8th Sector at 0.5 GeV

3.3 The Detector's Inefficiencies

As we have seen earlier on there are some concerns regarding the detector in certain areas which we will be focusing on. To have a first clue on the nature of those structures that appear on our $\sigma(\mathsf{p},\mathsf{m},\mathsf{l})$ we will take a closer look at them and compare them with the official MC simulation for ALICE.

3.3.1 The 8th Sector and the Phi Spikes

As we stated earlier we excluded these regions due to the fact they are systematic out-of-trends, to sustain this hypothesis we will focus on each of them to try to understand their nature. Comparing the measured resolution to to a full Monte Carlo simulation, including realistic digitisation and reconstruction, we can see in Figure 3.11 how the spikes (A) and the 8th Sector (B) are out of the simulation reproduction. Thus giving us an accordance of the simulation with our model of dependency, hinting it might really be an intrinsic characteristics of the detector.

3.3.2 The Z central bump and Spikes

The anomalies along Z are different form their counterparts on ϕ.

The Z Bump Starting from the bump in the central region: this strange feature extend through the two simulations made and to the measured simulation. We can see in Figure 3.12 how the simulation do not account for it, the Simulated Material might have a first clue on what is causing it and the Resolution has a remarkable Bump in the region. To the purpose of understanding what might cause the Bump we ran an analysis cutting in three parts the collision vertex position so as to have a third of the data central, left and right to the mean vertex position along Z. A non aligned Vertex might cause a slight bump in the region, but that is not the case as we can see in Figure 3.13.

The Z Spikes In a similar fashion the Spikes along Z are mismatching through our references. The peculiarity in this case is that the shape is somehow reproduced in the Simulation, but missing in the Material fast simulation. This might suggest that the fast simulation, despite a powerful tool for a qualitative characterisation
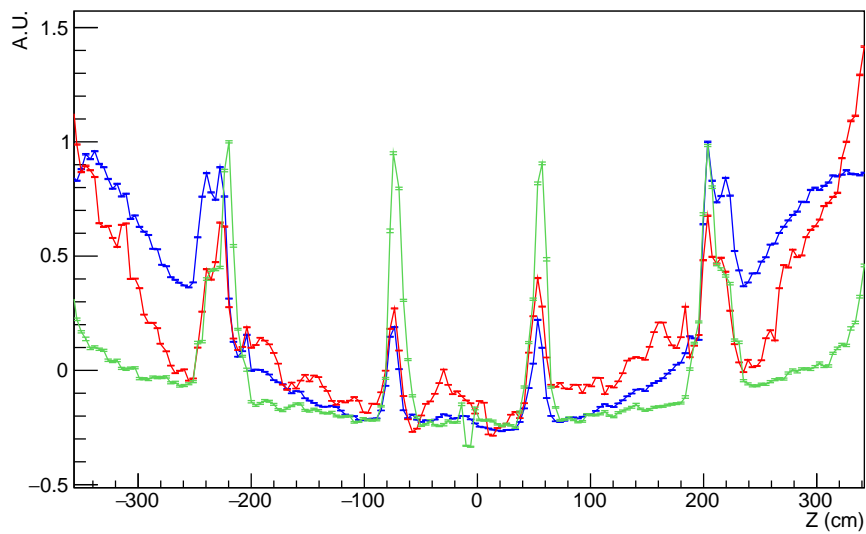
FIGURE 3.12: Along Z, the Resolution (Red), the Simulated Resolu-
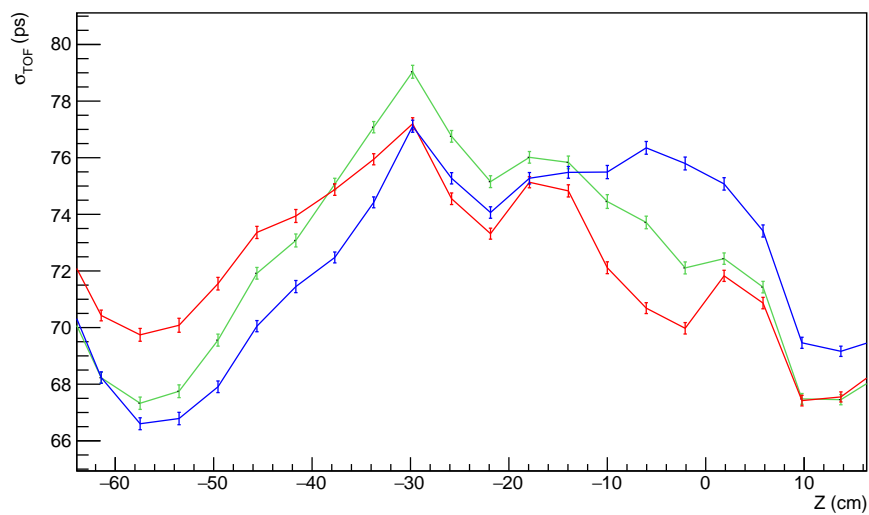tion (Blue) and the Simulated Material (Green)

FIGURE 3.13: The Z Bump close-up, central statistic (Green), right
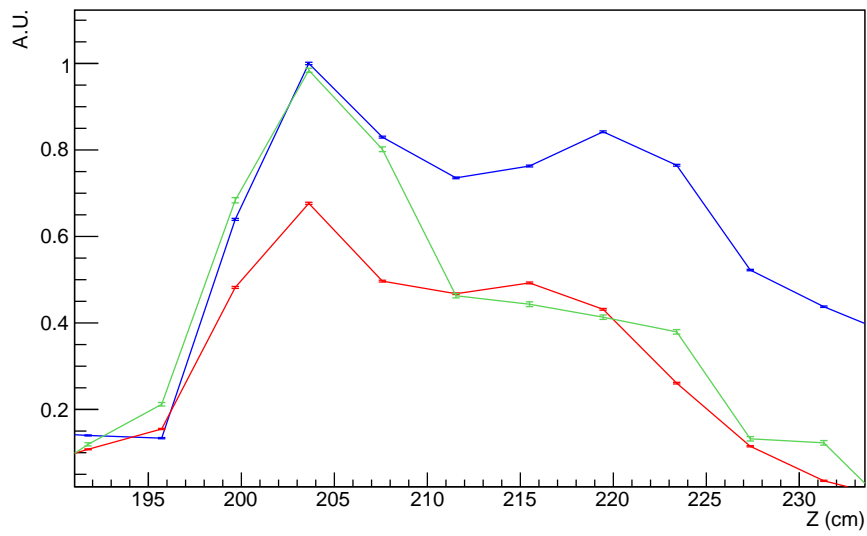side statistic (Red) and left side statistic (Blue)

FIGURE 3.14: A Spike along Z close-up, the Resolution (Red), the Simulated Resolution (Blue) and the Simulated Material (Green)

of material effects, did not account for all the details needed for a more detailed quantitative investigation.

Conclusions

The main accomplishment of this work is the statistical certainty of a dependence from momentum, material and track length of the TOF resolution. We think the latest version of the mapping formula

$$\sigma_{TOF} = \sqrt{c_{\mathsf{p},\mathsf{l}}^2 \frac{\mathsf{l}^2}{\mathsf{p}^4(1 + \frac{\mathsf{p}^2}{m_\pi^2})} + c_{\mathsf{m},\mathsf{p}}^2 \frac{\mathsf{m}^2}{\mathsf{p}^2}} \tag{3.8}$$

is still a very good starting point for further investigations that might assign to each and every channel an *a priori* resolution that might help weight the contributions or choose high precision tracks for specific precision studies, other than enhancing our capability to identify particles. The method developed in the analysis is very promising and extends our understanding of the resolution to the single channel.

The data at hand showed a strong evidence for our claims, even though it couldn't determine all the coefficients in our formula. The various cuts made along the analysis left too little events to run a sufficiently precise multi-differential analysis on the signals. Nonetheless new data will be available in the next months that might help develop an accurate model, which we encourage to pursue.

Overall this was the first multi-differential multi-dimensional analysis and it successfully brought to light many features of the TOF detector that will be very valuable for the ALICE experiment as it characterises in detail the performance of the TOF detector and therefore improve the knowledge of its response for physics analysis.

The analysis managed furthermore to find irregularities in the resolution patterns observed, many of which were compliant with our material dependence hypothesis on a qualitative level on a preliminary level, some others were instead unexpected. The main out-of-trends were found along the φ coordinate, which suggest there is a combination of two irregularities. The 8th sector seems to be pointing toward an electronic dysfunction which will be addressed by experts. The most interesting one is the modulation along sides of the MRPC chambers, which seems to mismatch a material correlation. This feature is confirmed by the comparison with a detailed simulation of the ALICE environment and should therefore be carefully addressed as to understand its origin.

Bibliography

[1] J. Rafelski; R. Hagedorn 1981 "From Hadron Gas to Quark Matter II" in H. Satz. Statistical mechanics of quarks and hadrons. North-Holland and Elsevier. pp. 253-272. ISBN 0-444-86227-7. CERN-TH-2969 (1980).

[2] Wolfgang Pauli 1940 "The Connection Between Spin and Statistics" in Physical Review.

[3] H.David Politzer. 1973 "Reliable Perturbative Results for Strong Interactions" In: Phys. Rev. Lett 30.1346.

[4] Frank Wilczek David J. Gross. 1973 "Ultraviolet Behavior of Non-Abelian Gauge Theories". In: Phys. Rev. Lett 30.1343.

[5] Siegfried Bethke. 2007 "Experimental Tests of Asymptotic Freedom Experimental Tests of Asymptotic Freedom". In: Prog. Part. Nucl. Phys. 58, pp. 351?386.

[6] Johann Rafelski Jean Letessier. 2002 "Hadrons and Quark-Gluon Plasma". In: Cambridge University Press, p. 91.

[7] Xiangdong Ji. "Quark-Gluon Plasma and the Early Universe". Lecture Notes.

[8] ALICE Collaboration. 1999 ALICE Technical Design Report of the Inner Tracking System (ITS). Tech. Rep. CERN.

[9] ALICE Collaboration. 1999 Technical Design Report of the Time Projection Chamber. Tech. Rep. CERN.

[10] PhD Thesis, Alma Mater Studiorum. Roberto Preghenella. 2009 "The Time-Of-Flight detector of ALICE at LHC: construction, test and commissioning with cosmic rays"

[11] Bachelor Thesis Alma Mater Studiorum, Francesca Sansavini 2016 "Misura della risoluzione temporale del sistema a Tempo di Volo (TOF) di ALICE in collisioni Pb-Pb a $\sqrt{s_{NN}}$ = 5.02 TeV"

[12] Physics Letters B Volume 696, Issues 1?2, 24 January 2011, Pages 30-39